ENSO constrains the magnitude of the Pattern Effect and increases the lower bound on climate sensitivity

Tyler Hanke[1*] and Cristian Proistosescu[1,2†]

[1*]Department of Climate, Meteorology, and Atmospheric Sciences, University of Illinois at Urbana Champaign, 506 S. Wright St., Urbana, 61801, IL, United States.
[2]Department of Earth Sciences and Environmental Change, University of Illinois at Urbana Champaign, 506 S. Wright St., Urbana, 61801, IL, United States.

*Corresponding author(s). E-mail(s): tjhanke2@illinois.edu;
Contributing authors: cristi@illinois.edu;
†These authors contributed equally to this work.

Abstract

As the spatial pattern of warming in sea surface temperatures evolves, it leads to changes in Earth's net radiative feedback and effective climate sensitivity. The magnitude of the change in feedback attributable to changes in *regional* temperature patterns is known as the "pattern effect". This pattern effect has been mostly attributed to variability in low cloud radiative effect (CRE), and exhibits significant variance in models while being poorly constrained from observations. Here we use ENSO as an emergent constraint on the pattern effect. We find strong linear relationships between modeled ENSO feedbacks and their respective pattern effects, especially for net CRE. Observed ENSO feedbacks lie within the middle of the model ensemble and suggest a pattern effect magnitude of $\mathbf{1.00 \pm 0.35}$ W/m$^{\mathbf{2}}$/K when calculated relative to preindustrial conditions. Model-simulated pattern effects also exhibit similar spatial distributions as the pattern diversity of ENSO, hinting at similar physics governing the two phenomena.

Keywords: El Nino Southern Oscillation, Pattern Effect, Emergent Constraint, Equilibrium Climate Sensitivity

1 Introduction

The response of Earth's climate to carbon dioxide (CO2) emissions is usually quantified using the sensitivity of global-mean surface temperatures due to a doubling of atmospheric carbon dioxide concentration, termed Equilibrium Climate Sensitivity (ECS), and denoted here by $\overline{T}_{2\times}$. ECS is usually estimated using a global-mean top-of atmosphere (TOA) energy budget framework. In this framework, the net TOA imbalance, $\Delta\overline{N}$ is separated into a net radiative forcing, $\Delta\overline{F}$, and a net radiative response, $\Delta\overline{R}$, the latter being driven by changes in global-mean temperature, $\Delta\overline{T}$, (Gregory et al., 2002; Gregory, 2004),

$$\Delta\overline{N} = \Delta\overline{F} + \Delta\overline{R} = \Delta\overline{F} + \lambda\Delta\overline{T}, \tag{1}$$

where the overline denotes a global-mean quantity, and λ denotes the global-mean net radiative feedback $\lambda = \Delta\overline{R}/\Delta\overline{T}$. At equilibrium, the net energy imbalance must be zero. Thus, by setting $\Delta\overline{N} = 0$ in equation (1), we can derive ECS as

$$ECS = \overline{T}_{2\times} = \frac{\Delta\overline{F}_{2\times}}{-\lambda}, \tag{2}$$

where $F_{2\times}$ is the radiative forcing associated with a doubling of atmospheric CO2 concentrations. Determining the exact value of ECS has important ramifications for policy, society, and human health, and there has therefore been significant effort in constraining its value from a variety of sources, including climate models, observations, and paleoclimate proxies (Intergovernmental Panel On Climate Change (IPCC), 2023).

In principle, one could estimate ECS from historical observations by first deriving a historical feedback, λ_{hist}, using equation (1) and historical observations of $\Delta\overline{N}, \Delta\overline{F}, \Delta\overline{T}$, and then using this in equation (2) to obtain an effective estimate of ECS (Gregory et al., 2002; Otto et al., 2013; Forster, 2016):

$$ECS_{\text{eff}} = \frac{\Delta\overline{F}_{2\times}}{-\lambda_{\text{hist}}}. \tag{3}$$

Discrepancies exist, however, when deriving ECS using the value of λ obtained from model simulations of historical and long-term climate states. In particular, λ has been found to have a time-varying component, becoming less negative over time (Armour et al., 2013). Since equilibrium feedbacks tend to be less negative than feedbacks acting over the historical period ($\lambda_{\text{hist}} < \lambda_{\text{eq}} < 0$), attempts to constrain ECS by utilizing equation (3) and a feedback estimate λ_{hist} drawn from observations of the present-day Earth's energy budget should lead to ECS estimates that are biased low (Forster, 2016; Proistosescu and Huybers, 2017; Armour, 2017; Knutti et al., 2017; Marvel et al., 2018; Andrews et al., 2018; Dessler, 2020). This is illustrated in Figure 1, where ECS estimates drawn from coupled quasi-equilibrated CMIP6 *abrupt-4xCO2* simulations (Eyring et al., 2016) are compared with ECS_{eff} from atmospheric models forced with observed historical boundary conditions (*amip-piForcing* simulations) (Andrews et al., 2018, 2022). To isolate only the impact on ECS due to changes in radiative feedbacks

on the ECS_{eff} estimates, each histogram uses the same radiative forcing (calculated for each CMIP6 model by Mark Zelinka [https://github.com/mzelinka/cmip56_forcing_feedback_ecs/blob/master/README.md]).

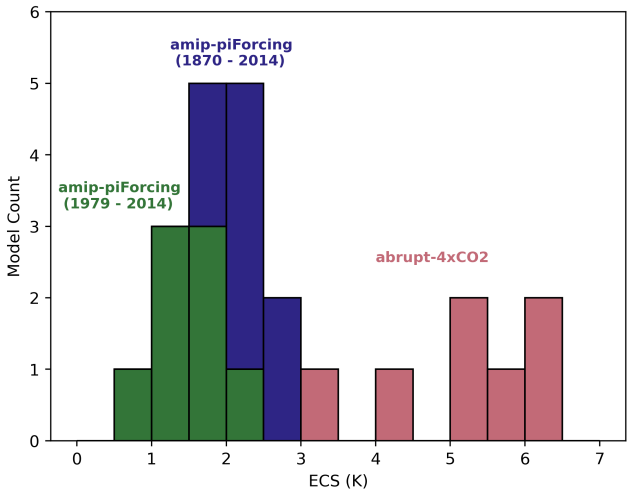

Fig. 1 Comparison of histogram ECS estimates from 8 CMIP6 models where the feedback parameter is obtained from (blue) *amip-piForcing* simulations from 1870 - 2014, (green) *amip-piForcing* simulations from 1979 - 2014, and (pink) *abrupt-4xCO2* simulations.

The inconstancy of the net feedback parameter is a result of the radiative response $\Delta\overline{R}$ - and thus the net radiative feedback - having a dependence upon both the magnitude of global-mean warming and regional sea surface temperature (SST) patterns, a dependence called "the pattern effect" (e.g. Andrews et al., 2015; Dong et al., 2019). The pattern effect can be quantified as the difference in net radiative feedback actuated by historical warming patterns, $T_{\text{hist}}(x)$ versus equilibrium warming patterns $T_{\text{eq}}(x)$, where x represents a latitude and longitude grid point,

$$\Delta\lambda = \lambda_{\text{eq}} - \lambda_{\text{hist}} = \frac{\Delta\overline{R}\left(\Delta T_{\text{eq}}\left(x\right)\right)}{\Delta\overline{T}_{\text{eq}}} - \frac{\Delta\overline{R}\left(\Delta T_{\text{hist}}\left(x\right)\right)}{\Delta\overline{T}_{\text{hist}}}, \tag{4}$$

Most of the difference in radiative feedbacks have been shown to be attributable to the cloud feedback component, $\Delta\lambda_{\text{cloud}}$ (Andrews et al., 2015; Zhou et al., 2016, 2017).

Thus, estimates of the radiative feedback acting over the historical period are not sufficient to infer equilibrium climate sensitivity. One also needs an estimate of the *change* in feedback, $\Delta\lambda$. (Sherwood et al., 2020). Unfortunately, $\Delta\lambda$, and especially $\Delta\lambda_{\text{cloud}}$, are poorly constrained, with models exhibiting a large spread. Consequently, direct estimates from Earth's present-day energy budget so far only constrain the lower-bound of ECS (Sherwood et al., 2020). Some studies have attempted to place observational constraints on the pattern effect - Myers et al. (2021), which uses a blend

of satellite records and the cloud controlling factor (CCF) formalism (Klein et al., 2017), finds values cloud feedback and net feedback pattern effects for the 1982-2018 interval of $\Delta\lambda_{\text{cloud}} = 0.78 \pm 0.21$ W/m^2/K and $\Delta\lambda = 1.86 \pm 0.45$ W/m^2/K, respectively. However, Myers et al. (2021) finds significant uncertainty due to disparity between the meteorological changes across the different reanalysis datasets used. Andrews et al. (2022) also places an observational constraint on the pattern effect by deriving λ_{hist} from observed $\Delta\overline{N}, \Delta\overline{F}, \Delta\overline{T}$ over the 1985-2015 interval and computing the pattern effect magnitude to be 0.8 ± 1.0 W/m^2/K (0.4 ± 1.1 W/m^2/K using the 1871-2014 interval). The authors note that these estimates show strong agreement between these observationally constrained quantities and GCM simulations, but there remains the issue of a large uncertainty interval.

Here, we show that there is a strong relationship between the El Nino Southern Oscillation (ENSO) radiative feedbacks and the pattern effect, and use this relationship to derive an emergent constraint on the cloud and net feedback pattern effects that substantially reduces uncertainty in the pattern effect. We further show that relationship arises from the similarity in the spatial patterns of both phenomena, and point to similarity changes in atmospheric stability as a potential pathway that the relationship emerges. We then demonstrate the implications of this emergent constraint on ECS. Finally, we argue that a longer period of overlap between model simulations and satellite observations would yield progressively tighter constraints.

2 Results

2.1 ENSO Patterns and Feedbacks

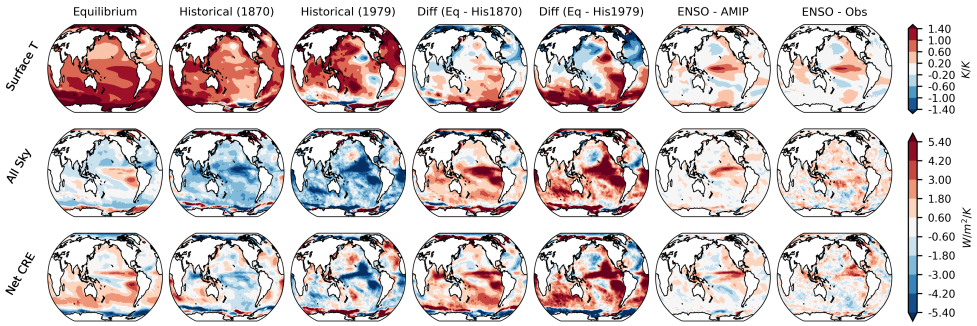

Fig. 2 Comparison of spatial patterns for (first row) surface temperature, (second row) all-sky feedbacks, and (third row) net cloud feedbacks under equilibrium, historical (1870 - 2014 and 1979 - 2014), pattern effect, and ENSO feedback. Maps shown are the ensemble average over the 8 available climate models, except for the last column which is computed from observations (see Methods).

ENSO is the dominant driver of SST and TOA radiation anomalies on interannual time scales, and thus also dominates the relatively short observational record of net TOA energy storage anomalies (Johnson and Birnbaum, 2017). Additionally,

ENSO is a relatively well understood and comprehensively investigated phenomenon (e.g. review by McPhaden, 2020). These factors make ENSO a prime-candidate for observational constraints of radiative feedbacks. Indeed, past studies have found that ENSO variability could be used as a potential "emergent constraint" (Klein and Hall, 2015) on cloud feedbacks. Lutsko (2018) and Lutsko and Takahashi (2018) found strong linear relationships ($r^2 \sim 0.6$) between cloud radiative feedbacks at ENSO time scales and long-term cloud radiative feedbacks in climate models, although their potential emergent constraint require much longer observational records than currently available.

The similarity between ENSO-driven SST variations and the SST changes associated with the pattern effect suggests ENSO could offer a tighter constraint on the pattern effect $\Delta\lambda$ than on the net equilibrium feedback λ_{eq}. Figure 2 (top row) compares ensemble-mean patterns of equilibrium, historical and ENSO SSTs. The ensemble-mean equilibrium SST patterns show enhanced warming in the east Pacific and southern Ocean, whereas observed SST patterns spanning both the entire CMIP historical simulations (1870-2014) and the AMIP interval (1979-2014) show little warming and even cooling trends in the east Pacific and southern Ocean. When taking the difference between the equilibrium and historical period temperature patterns, we find that the pattern of change displays strong gradients in the equatorial Pacific, similar to the ENSO SST patterns (Fig. 2) (r = 0.5 - 0.7 for simulated ENSO and r = 0.5 - 0.8 for observed ENSO patterns between 10N to 10S [see also Table 1 and Figure 1]). Since the pattern effect (Eqn. 4) is driven by the change in SST patterns between historical and equilibrium states, and the higher correlation within the nino regions, this similarity suggests ENSO as a potential emergent constraint.

When defining ENSO-related radiative feedbacks, care must be taken as the ENSO radiative response leads and lags changes in the nino3.4 index, and is nearly zero when computed in phase with nino3.4, i.e. at zero lag (Fig. 2, see also Proistosescu et al., 2018; Ceppi and Fueglistaler, 2021). We thus define the ENSO radiative feedback by considering the deseasonalized, detrended monthly-mean lagged TOA response to nino3.4 changes, and taking the maximum global-mean positive radiative response for each individual climate model - hereafter referred to as just the ENSO feedback, λ_{ENSO} (see Methods).

We find that all-sky radiation feedbacks, dominated by CRE changes, exhibit strong damping feedbacks throughout the east-central tropical Pacific during the historical time period, and that these feedbacks switch to amplifying feedbacks under quasi-equilibrium conditions. Taking the difference between these two yields a change in feedback that is similar to feedbacks induced by ENSO, with particularly strong positive cloud feedbacks in the equatorial and sub-tropical East Pacific, primarily in regions of high climatological low cloud cover.

2.2 ENSO-based Emergent Constraints

We now turn to using λ_{ENSO} as an emergent constraint. Since no two ENSOs have exactly the same pattern, the net ENSO feedback will change depending on the time period considered (Chao et al., 2022). To avoid issues arising from period-dependence

we compute λ_{ENSO} using the period of overlap between AMIP models and CERES observations, namely 2001-2014.

We find a significant correlation (tested with a leave-one-out validation method) between the ENSO feedback λ_{ENSO} in *amip* simulations and both the cloud feedback pattern effect, $\Delta\lambda_{\mathrm{cloud}}$ ($0.69 < r < 0.98$), and the net feedback pattern effect $\Delta\lambda$ ($0.49 < r < 0.98$) across the 8 available CMIP6 *amip-piForcing* simulations (Fig. 3). Additionally, estimates of both cloud and net feedback pattern effects and their ENSO feedbacks inferred from observations lie within the middle of the model ensemble. We see these results regardless of the model starting year used (1870 or 1979) in the *amip-piForcing* to define $\Delta\lambda$. We find a pattern effect of 1.00 ± 0.35 W/m^2/K using the 1870-2014 time period and 1.90 ± 0.66 W/m^2/K using the 1979-2014 time period. These estimates are within their respective model ensemble range, and their expected values are within the upper-limits of the estimates used in both the Sherwood et al. (2020) assessment (0.5 ± 0.5 W/m^2/K) and the Andrews et al. (2022) study (0.7 ± 0.47 W/m^2/K for 1871-2010 and 1.38 ± 0.75 W/m^2/K for 1981-2010), but with tighter uncertainty intervals.

The fact that we only used 14 years of 23 years available in the CERES records leads to a large uncertainty in the observed ENSO feedback, and a large uncertainty in the resulting pattern effect. Using the full CERES period would result in tighter estimate of λ_{ENSO} and a tighter constraint on the pattern effect of 0.80 ± 0.22 W/m^2/K for 1870-2014 and 1.51 ± 0.42 W/m^2/K for 1979-2014 (dashed PDFs in Fig. 3). However, it is unclear if the emergent constraint λ_{ENSO} and $\Delta\lambda$ would change if λ_{ENSO} was computed using 2001-2024 data. We argue that a straightforward way to improve constraints on the pattern effect is to have sufficient climate models with AMIP simulations that cover the entire CERES interval, as proposed in CERESMIP (Schmidt et al., 2023). We also compared the observed ENSO feedbacks using the full CERES period and those calculated using the entire AMIP interval to test the sensitivity of the pattern effect-ENSO relationship to the time interval used on the ENSO feedbacks (Figure 3). Although there exists a uniformly negative bias in the magnitude of the ENSO feedbacks - attributable to ENSO clear-sky feedbacks - the behavior across lags is consistent, particularly for cloud feedbacks.

Much of the strong global-mean correlation between ENSO feedbacks and the pattern effect stems from cloud variability. The net CRE pattern effect and net CRE ENSO feedback are even more highly correlated than for all-sky conditions ($r = 0.93$) for both *amip-piForcing* time periods. In contrast, the clear-sky pattern effect and clear-sky ENSO feedback instead are weakly anti-correlated ($r < -0.4$) - however, the clear sky pattern effect is expected to be a smaller component of the pattern effect, relative to the cloud feedback (Andrews et al., 2015).

To understand the different cloud radiative processes contributing to these results, we decompose the net cloud feedbacks into SW and LW CRE. It is evident that regardless of the starting year for the *amip-piForcing* simulations, SW CRE ENSO feedbacks are highly positively correlated ($r = 0.9$ for entire simulation, $r = 0.82$ for only AMIP internal) while LW CRE ENSO feedbacks are only moderately anticorrelated

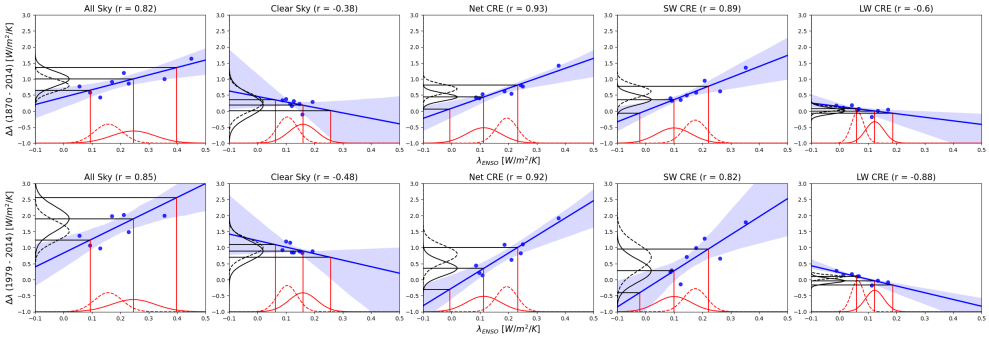

Fig. 3 Correlation analysis between within model pattern effect ($\Delta\lambda$) and ENSO feedbacks ($\Delta\lambda_{ENSO}$) for different types of radiation using (top row) the entire CMIP interval (1870 - 2014) and (bottom row) the AMIP interval (1979 - 2014) in 8 CMIP6 models. The blue-shaded region indicates the 95-percentile confidence interval of the regression equation. Included on the x-axis is a PDF estimate of ENSO feedbacks and on the y-axis the inferred observational pattern effect from a kernel density estimate. Both PDFs are obtained using (solid) 2001 - 2014 and (dashed) 2001 - 2023 CERES EBAF data. The red vertical lines represent the 95-percentile values in the 2001 - 2014 ENSO feedbacks, and the black horizontal lines represent the interpreted 95-percentile values of the pattern effect using the regression equation.

($r = -0.6$) with their respective pattern effects. Interestingly, though, the anticorrelation between LW CRE ENSO feedbacks and model pattern effects for simulations over the AMIP interval (1979 - 2014) is high ($r = -0.9$).

To understand the origin of the tight relationship between λ_{ENSO} and $\Delta\lambda$, we examine the full spatial pattern of the two feedbacks for each model. Figure 4 depicts the pattern effect (from both 1870 and 1979 to 2014) and ENSO cloud radiative feedbacks for each model in the ensemble and those derived from observational data. Note that these are AMIP simulations, so all models are driven by observed SST patterns. Thus, all differences in the radiative feedback comes from the different radiative response to identical SST anomalies, and not from differences in how coupled models simulate ENSO SST patterns. By plotting the strength of the net CRE pattern effect and ENSO feedbacks as a function of longitude in the nino3 and nino4 regions (Fig 5), we can clearly that the models can be broadly classified into three broad categories: models with strong pattern effects that peak in the eastern Pacific also tend to have strong eastern Pacific ENSO feedbacks (CESM2, MIROC6, TaiESM1); models with strong pattern effects that peak in the central Pacific tend to have strong central Pacific ENSO feedbacks (CanESM5, IPSL-CM6A-LR, MRI-ESM2-0); and models with weak pattern effects tend to also have weak ENSO feedbacks (CNRM-CM6-1, HadGEM3-GC31-LL). We also highlight a potential physical explanation for the strong relationship between ENSO and the pattern effect for net CRE by looking at the spatial distribution of changes in atmospheric stability (estimated inversion strength, EIS) for both, which has been shown in previous studies that, when combined with surface temperature, dominates variability in the global radiation budget and has been used as observational constraints on the cloud feedback P. Ceppi (2019); Ceppi and Nowack (2021).

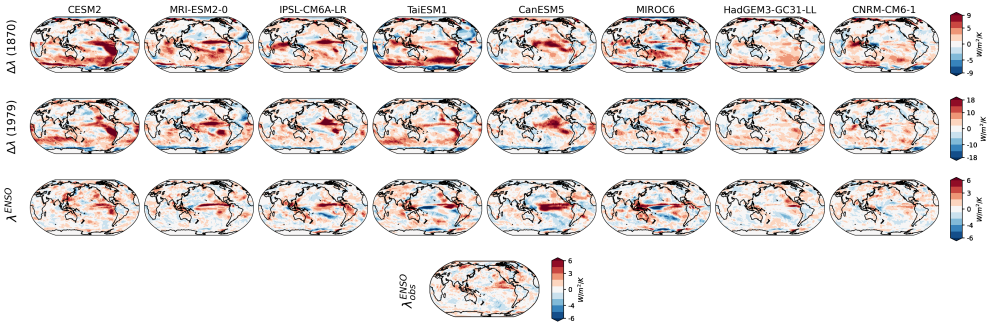

Fig. 4 Comparison of 8 CMIP6 model spatial patterns for net cloud pattern effects using (first row) the entire CMIP interval (1870 - 2014) and (second row) the AMIP interval (1979 - 2014). These are compared to (third row) AMIP interval modeled net cloud ENSO feedbacks and (fourth row) the observed net cloud ENSO feedback.

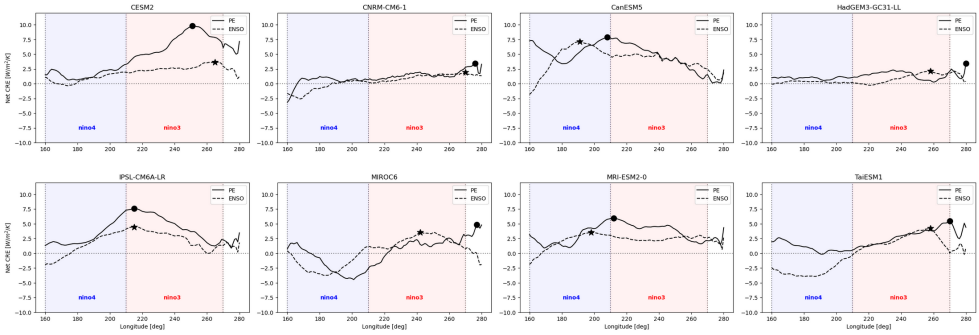

Fig. 5 Comparison between equatorial (10N to 10S) ENSO (dashed) and pattern effect-induced (solid) net cloud radiative feedback anomalies as a function of longitude for 8 CMIP6 models. Also indicated are the nino3 (red) and nino4 (blue) regions.

We find that EIS responds strongly in the east and central Pacific, in particularly the stratocumulus decks, to ENSO and pattern effect temperature patterns.

2.3 An Updated ECS Posterior

We finally turn to the implications of using this ENSO-based emergent constraint on the pattern effect on ECS. In Figure 6 we attempt to calculate the historical and the full posterior ECS distributions calculated in Sherwood et al. (2020) with our emergent constraint and compare to ECS distributions using the previous estimates of the pattern effect.

When the Sherwood full posterior of ECS is updated with the ENSO-based emergent constraints on the pattern effect magnitude, ECS less than $2K$ is essentially ruled out as a possibility. ECS evaluated for the conditions of the Sherwood uniform λ baseline $(3.1[2.5, 3.9]K)$ shifts under the higher $\Delta\lambda$ to higher sensitivities $(3.5[2.9, 4.4]K$

for 2001-2014 and $3.4[2.8, 4.2]K$ for 2001-2023). In fact, despite the more tightly constrained pattern effect, there is little to no impact on the uncertainty interval for ECS, depending upon the time period chosen for inclusion of the CERES data.

Upon examining the historical likelihood, we see why the more tightly constrained pattern effect from this study yields little impact on ECS uncertainty. This is because the significant increase in the median pattern effect magnitude shifts the entire likelihood function to higher ECS, resulting more plausibility for extreme ECS (e.g. $P(14K)$ ¿ $P(4K)$) and much higher uncertainty in the historical likelihood. We know from Sherwood et al. (2020) historical evidence provides a weak constraint on the upper bound of ECS, and so by shifting the historical likelihood as a whole to higher ECS results in an even weaker constraint to the upper bound of the full ECS posterior. Therefore, this large shift in the central estimate of the pattern effect negates the reduction in uncertainty in $\Delta\lambda$, thus dragging ECS to higher sensitivities but with little to no uncertainty reduction.

3 Discussion

In this study we show that the radiative response to ENSO provides an observational constraint on the pattern effect and thereby long-term radiative feedbacks. By using a correlation analysis framework, we conclude that there is a strong linear relationship between ENSO radiative feedbacks and the pattern effect, and are able to use observational priors to estimate the most likely pattern effect range to be 1.00 ± 0.35 W/m^2/K when using the full 1870-2014 time interval and 1.90 ± 0.66 W/m^2/K when using the 1979-2014 time interval. This estimate lies on the upper end of the ranges given in Sherwood et al. (2020) and Andrews et al. (2022), but with significantly reduced uncertainty. Additionally, as more observational satellite data are used to derive the ENSO feedbacks, the expected value of the pattern effect becomes more agreeable with their previous pattern effect ranges but with even tighter constraints.

The relationship between ENSO feedbacks and pattern effect is driven by a strong correlation between cloud radiative feedbacks, and models with strong pattern effects in either the East or Central Pacific also have ENSO feedbacks concentrated in, respectively, the East or the Central Pacific. Conversely, models with weak pattern effects exhibit weak ENSO feedbacks. From this, we conclude that model simulated pattern effects have similar spatial diversity as ENSO.

We find that the relationship is driven by similarity in the model radiative response to ENSO SST anomalies and the radiative response to changing SST patterns between historical and future climate states. Additionally, we have shown that both ENSO and the pattern effect exhibit similar spatial distributions of EIS changes, from which we conclude that EIS is another potential driver of the ENSO-based emergent constraint relationship. A deeper investigation using radiative kernels for each respective model to more fully understand the contributions of SST and EIS changes to this emergent constraint is warranted.

We then investigate the impact of this ENSO-based emergent constraint on climate sensitivity by updating the pattern effect magnitude in the Sherwood et al. (2020) historical likelihood and full posterior for ECS. We find that ECS shifts to higher

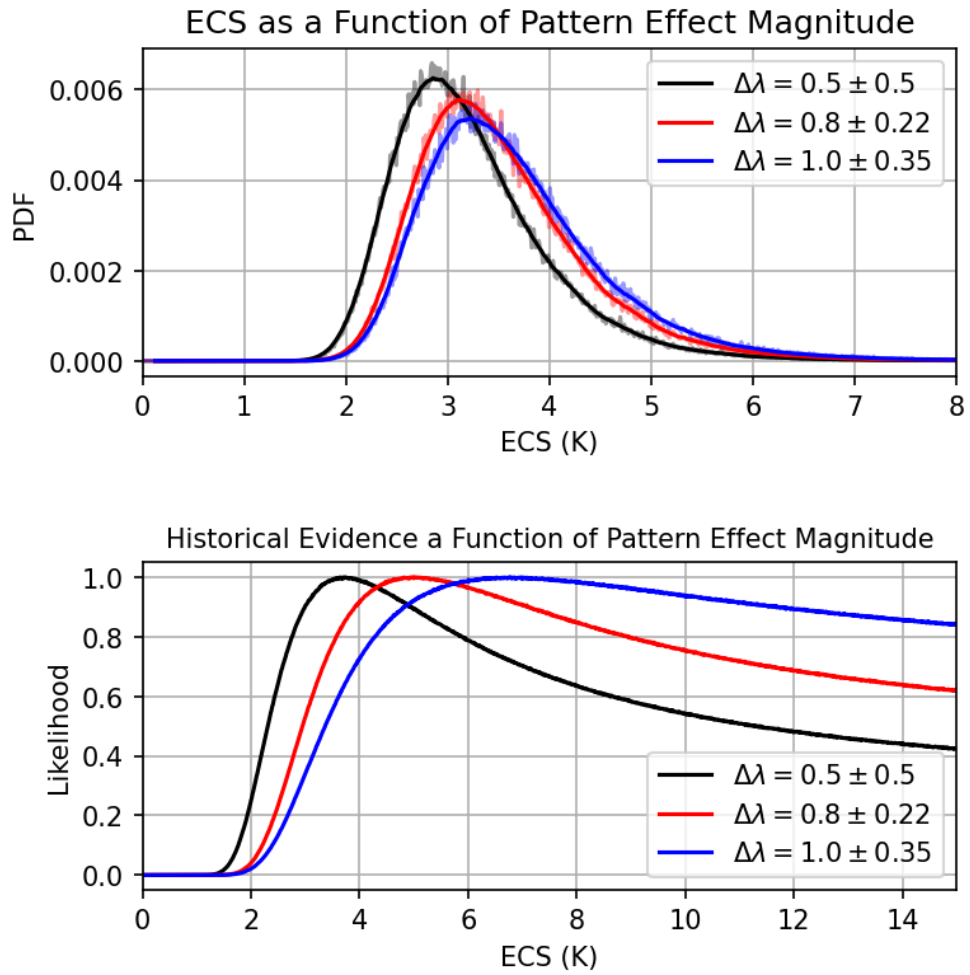

Fig. 6 Comparison of the full (normalized) ECS posterior distribution and historical likelihood when calculated with (black) the Sherwood et al. (2020), (blue) 2001-2014 ENSO emergent constraint, and (red) 2001-2023 ENSO emergent constraint pattern effect estimates.

sensitivities (median ECS shifts from $3.2K$ to $3.5K$) due to the increased pattern effect magnitude and essentially rules out sensitivities less than $2K$, but with no impact to the uncertainty in ECS despite a much more tightly constrained pattern effect. This is due to the substantial increase in the central estimate of $\Delta\lambda$ negating the decreased uncertainty within the historical likelihood, suggesting historical evidence provides an even weaker constraint on the upperbound of ECS than was determined in Sherwood et al. (2020).

While the emergent constraint is apparently strong, it is so far only based on a small set of climate models (8), and on a relatively short period of overlap between AMIP

simulations and CERES data (2001-2014). A straightforward way to improve both the confidence in this emergent constraint and to reduce the uncertainty in the pattern effect is for more models to run *amip-piForcing* simulations (which would increase the number of models available), and for AMIP simulations to be extended over the entire duration of the CERES interval (Schmidt et al., 2023). We also acknowledge that there is a dependency for the magnitude of the pattern effect upon the SST dataset prescribed when running the piForcing simulations Andrews et al. (2022). Simulations prescribed with the HadISST1 dataset Rayner et al. (2003) have shown the pattern effect magnitude to be much smaller than those using the AMIP II SST boundary conditions, which may have an impact on the strength of the relationship between the pattern effect and ENSO feedbacks depicted in this paper. Further investigation into the structural dependency of the emergent constraint on the prescribed SST dataset is warranted.

4 Online Methods

4.1 Observed Radiation Fluxes

Readily available daily and monthly-mean all-sky and clear-sky radiation fluxes are obtained from the National Aeronautics and Space Administration (NASA) Clouds and the Earth's Radiant Energy System (CERES) Energy Balance and Filled (EBAF) Edition 4.1 dataset (Loeb et al., 2018), the flagship data product for satellite observations of the Earth's radiative budget that may be accessible from the CERES data product store https://ceres.larc.nasa.gov/data/. By subtracting the clear-sky fluxes from all-sky fluxes, we are able to obtain the net CRE radiation field.

4.2 General Circulation Models

Following the procedures used to quantify the pattern effect in Andrews et al. (2018) and Andrews et al. (2022), we use GCM data from 8 CMIP6 models (CanESM5, CESM2, CNRM-CM6-1, HadGEM3-GC31-LL, IPSL-CM6A-LR, MIROC6, MRI-ESM2-0, and TaiESM1) that are available on the ESGF CMIP6 database (https://esgf-node.llnl.gov/search/cmip6/). These models were selected as they are the only models that have run *amip-piForcing* simulations (Webb et al., 2017), which are run with prescribed SST patterns but with external forcings held fixed at pre-industrial control levels and simulations are run for the 1870 - 2014 time period. This feature of the *amip-piForcing* simulations make it preferable to use over *amip* simulations in calculating the pattern effect because it constrains the influence of external forcings and makes the historical feedback parameter more dependent upon the simulated surface temperature patterns (Andrews et al., 2022).

4.3 Historical Feedbacks

To obtain the historical radiative feedback parameter (λ_{hist}), we regress annual-mean TOA radiation against global and annual-mean surface temperature data in the *amip-piForcing* simulations,

$$\lambda_{\text{hist}}(x,y) = \frac{\Delta R_{\text{amip-piForcing}}(x,y,t)}{\Delta T_{\text{amip-piForcing}}(t)} \tag{5}$$

4.4 Equilibrium Feedbacks

For estimating the equilibrium radiative feedback parameter (λ_{eq}), we perform the same regression technique described above and use the aforementioned models' *abrupt-4xCO2* simulations, which abruptly quadruple atmospheric CO2 concentrations and allow to system to quasi-equilibrate over a 150-year simulation. To reduce the influence of model spin-up and high-frequency variability, as a pre-processing step we discard the initial 20 years of each simulation and use pentadal-mean surface temperature and TOA radiation data,

$$\lambda_{\text{eq}}(x,y) = \frac{\Delta R_{4\times CO_2}(x,y,t)}{\Delta T_{4\times CO_2}(t)} \tag{6}$$

4.5 ENSO Radiative Feedbacks

To obtain the observed and simulated ENSO radiative feedback (λ_{ENSO}), we use the CERES-EBAF v4.1 (see Observed Radiation Fluxes) and the ERA5 reanalysis dataset Hersbach et al. (2020) and each model's *amip* simulation to regress observed and simulated top-of-atmosphere radiation onto the observed and simulated nino3.4 index time-series. For the simulated ENSO feedbacks, the choice of using *amip* simulations was made to retain historical forcing values, which allows for a better comparison to the observationally-derived ENSO feedbacks. To ensure we also account for any latent relationships between ENSO surface temperature patterns and atmospheric radiation, we shift the nino3.4 time-series by various lags to perform lagged linear regression,

$$\lambda_{\text{ENSO}}(x,y,\tau) = \frac{\Delta R_{\text{amip}}(x,y,t)}{\Delta \text{nino3.4}_{\text{amip}}(t-\tau)} \tag{7}$$

4.6 Probability Density and Kernel Density Estimates

In constructing our emergent constraint, we use probability density and kernel density estimation to visualize the uncertainty in magnitude of the observed pattern effect and ENSO feedbacks. The probability density estimate for the ENSO feedback is obtained using the 1-σ and mean value of the lagged linear regression, evaluated on the interval $[-0.1, 0.5]$ W/m^2/K .

Kernel density estimation, which is a non-parametric statistical method of generating a PDF using a Gaussian kernel, was used to estimate the magnitude and uncertainty in the observed pattern effect using the observed ENSO feedback and emergent constraint relationship. To do this, we use 10,000 random draws from the observed ENSO feedback distributions and from a regression of the simulated pattern effect magnitudes and ENSO feedbacks. We then use Scipy's Gaussian kernel density estimation function to obtain the KDE evaluated on the interval $[-1, 3]$ W/m^2/K .

Acknowledgements. TJH was supported by NASA grant number 80NSSC21K1043. CP was supported by DOE RGMA grant number SC0022110, and a NASA grant number 80NSSC21K1043. We would also like to give special thanks to Vince Cooper for running the full ECS posterior and ECS historical likelihood simulations using the ENSO emergent constraints. We would also like to thank fruitful conversations at the Global Cupcake Meeting in Reading.

Declarations

Funding: CP was supported by DOE RGMA grant #DE-SC0022110 and NASA New Investigator Program grant # 80NSSC21K1043. TJH was supported by NASA New Investigator Program grant # 80NSSC21K1043.

The authors declare they have no conflicting or competing interest.

Author contributions: CP and TJH developed the methodology and analyzed the data. TJH wrote the manuscript. CP edited the manuscript.

Data availability: Model data is available from the public CMIP archive: https://aims2.llnl.gov/search. CERES EBAF data is available from the public CERES repository: https://ceres.larc.nasa.gov/data/.

Code availability: https://github.com/TylerHanke/enso-as-an-emergent-constraint

References

Andrews, T., Bodas-Salcedo, A., Gregory, J.M., Dong, Y., Armour, K.C., Paynter, D., Lin, P., Modak, A., Mauritsen, T., Cole, J.N.S., Medeiros, B., Benedict, J.J., Douville, H., Roehrig, R., Koshiro, T., Kawai, H., Ogura, T., Dufresne, J., Allan, R.P., Liu, C.: On the Effect of Historical SST Patterns on Radiative Feedback. Journal of Geophysical Research: Atmospheres **127**(18), 2022–036675 (2022) https://doi.org/10.1029/2022JD036675 . Accessed 2023-11-29

Armour, K.C., Bitz, C.M., Roe, G.H.: Time-Varying Climate Sensitivity from Regional Feedbacks. Journal of Climate **26**(13), 4518–4534 (2013) https://doi.org/10.1175/JCLI-D-12-00544.1 . Accessed 2023-11-01

Andrews, T., Gregory, J.M., Paynter, D., Silvers, L.G., Zhou, C., Mauritsen, T., Webb, M.J., Armour, K.C., Forster, P.M., Titchner, H.: Accounting for Changing Temperature Patterns Increases Historical Estimates of Climate Sensitivity. Geophysical Research Letters **45**(16), 8490–8499 (2018) https://doi.org/10.1029/2018GL078887 . Accessed 2022-07-15

Andrews, T., Gregory, J.M., Webb, M.J.: The Dependence of Radiative Forcing and Feedback on Evolving Patterns of Surface Temperature Change in Climate Models. Journal of Climate **28**(4), 1630–1648 (2015) https://doi.org/10.1175/JCLI-D-14-00545.1 . Accessed 2022-07-13

Armour, K.C.: Energy budget constraints on climate sensitivity in light of inconstant climate feedbacks. Nature Climate Change **7**(5), 331–335 (2017) https://doi.org/10.1038/nclimate3278 . Accessed 2023-11-01

Ceppi, P., Fueglistaler, S.: The El Niño–Southern Oscillation Pattern Effect. Geophysical Research Letters **48**(21) (2021) https://doi.org/10.1029/2021GL095261 . Accessed 2022-06-10

Chao, L., Muller, J.C., Dessler, A.E.: Impacts of the Unforced Pattern Effect on the Cloud Feedback in CERES Observations and Climate Models. Geophysical Research Letters **49**(2), 2021–096299 (2022) https://doi.org/10.1029/2021GL096299 . Accessed 2024-11-04

Ceppi, P., Nowack, P.: Observational evidence that cloud feedback amplifies global warming. Proceedings of the National Academy of Sciences **118**(30), 2026290118 (2021) https://doi.org/10.1073/pnas.2026290118 . Accessed 2021-07-27

Dessler, A.E.: Potential Problems Measuring Climate Sensitivity from the Historical Record. Journal of Climate **33**(6), 2237–2248 (2020) https://doi.org/10.1175/JCLI-D-19-0476.1 . Accessed 2022-11-07

Dong, Y., Proistosescu, C., Armour, K.C., Battisti, D.S.: Attributing Historical and Future Evolution of Radiative Feedbacks to Regional Warming Patterns using a Green's Function Approach: The Preeminence of the Western Pacific. Journal of Climate **32**(17), 5471–5491 (2019) https://doi.org/10.1175/JCLI-D-18-0843.1 . Accessed 2021-08-25

Eyring, V., Bony, S., Meehl, G.A., Senior, C.A., Stevens, B., Stouffer, R.J., Taylor, K.E.: Overview of the Coupled Model Intercomparison Project Phase 6 (CMIP6) experimental design and organization. Geoscientific Model Development **9**(5), 1937–1958 (2016) https://doi.org/10.5194/gmd-9-1937-2016 . Accessed 2023-08-28

Forster, P.M.: Inference of Climate Sensitivity from Analysis of Earth's Energy Budget. Annual Review of Earth and Planetary Sciences **44**(1), 85–106 (2016) https://doi.org/10.1146/annurev-earth-060614-105156 . Accessed 2022-11-11

Gregory, J.M.: A new method for diagnosing radiative forcing and climate sensitivity. Geophysical Research Letters **31**(3), 03205 (2004) https://doi.org/10.1029/2003GL018747 . Accessed 2023-06-05

Gregory, J.M., Stouffer, R.J., Raper, S.C.B., Stott, P.A., Rayner, N.A.: An Observationally Based Estimate of the Climate Sensitivity. Journal of Climate **15**(22), 3117–3121 (2002) https://doi.org/10.1175/1520-0442(2002)015⟨3117:AOBEOT⟩2.0.CO;2 . Accessed 2024-11-04

Hersbach, H., Bell, B., Berrisford, P., Hirahara, S., Horányi, A., Muñoz-Sabater, J., Nicolas, J., Peubey, C., Radu, R., Schepers, D., Simmons, A., Soci, C., Abdalla,

S., Abellan, X., Balsamo, G., Bechtold, P., Biavati, G., Bidlot, J., Bonavita, M., Chiara, G.D., Dahlgren, P., Dee, D., Diamantakis, M., Dragani, R., Flemming, J., Forbes, R., Fuentes, M., Geer, A., Haimberger, L., Healy, S., Hogan, R.J., Hólm, E., Janisková, M., Keeley, S., Laloyaux, P., Lopez, P., Lupu, C., Radnoti, G., Rosnay, P., Rozum, I., Vamborg, F., Villaume, S., Thépaut, J.-N.: The era5 global reanalysis. Quarterly Journal of the Royal Meteorological Society **146**(730) (2020) https://doi.org/10.1002/qj.3803 . Accessed 2020-05-17

Intergovernmental Panel On Climate Change (IPCC): Climate Change 2021 – The Physical Science Basis: Working Group I Contribution to the Sixth Assessment Report of the Intergovernmental Panel on Climate Change, 1st edn. Cambridge University Press, ??? (2023). https://doi.org/10.1017/9781009157896

Johnson, G.C., Birnbaum, A.N.: As El Niño builds, Pacific Warm Pool expands, ocean gains more heat: ENSO, the Ocean, and Earth's Energy Uptake. Geophysical Research Letters **44**(1), 438–445 (2017) https://doi.org/10.1002/2016GL071767 . Accessed 2021-01-03

Klein, S.A., Hall, A.: Emergent Constraints for Cloud Feedbacks. Current Climate Change Reports **1**(4), 276–287 (2015) https://doi.org/10.1007/s40641-015-0027-1 . Accessed 2023-03-03

Klein, S.A., Hall, A., Norris, J.R., Pincus, R.: Low-Cloud Feedbacks from Cloud-Controlling Factors: A Review. Surveys in Geophysics **38**(6), 1307–1329 (2017) https://doi.org/10.1007/s10712-017-9433-3 . Accessed 2021-08-28

Knutti, R., Rugenstein, M.A.A., Hegerl, G.C.: Beyond equilibrium climate sensitivity. Nature Geoscience **10**(10), 727–736 (2017) https://doi.org/10.1038/ngeo3017 . Accessed 2024-11-04

Loeb, N.G., Doelling, D.R., Wang, H., Su, W., Nguyen, C., Corbett, J.G., Liang, L., Mitrescu, C., Rose, F.G., Kato, S.: Clouds and the Earth's Radiant Energy System (CERES) Energy Balanced and Filled (EBAF) Top-of-Atmosphere (TOA) Edition-4.0 Data Product. Journal of Climate **31**(2), 895–918 (2018) https://doi.org/10.1175/JCLI-D-17-0208.1 . Accessed 2022-10-11

Lutsko, N.J., Takahashi, K.: What Can the Internal Variability of CMIP5 Models Tell Us about Their Climate Sensitivity? Journal of Climate **31**(13), 5051–5069 (2018) https://doi.org/10.1175/JCLI-D-17-0736.1 . Accessed 2022-11-07

Lutsko, N.J.: The Relationship Between Cloud Radiative Effect and Surface Temperature Variability at El Niño-Southern Oscillation Frequencies in CMIP5 Models. Geophysical Research Letters **45**(19) (2018) https://doi.org/10.1029/2018GL079236 . Accessed 2022-07-15

McPhaden, M.J. (ed.): El Niño Southern Oscillation in a Changing Climate, First edition edn. Geophysical monograph series. Wiley-American Geophysical Union,

Hoboken, NJ (2020)

Marvel, K., Pincus, R., Schmidt, G.A., Miller, R.L.: Internal Variability and Disequilibrium Confound Estimates of Climate Sensitivity From Observations. Geophysical Research Letters **45**(3), 1595–1601 (2018) https://doi.org/10.1002/2017GL076468 . Accessed 2022-11-07

Myers, T.A., Scott, R.C., Zelinka, M.D., Klein, S.A., Norris, J.R., Caldwell, P.M.: Observational constraints on low cloud feedback reduce uncertainty of climate sensitivity. Nature Climate Change **11**(6), 501–507 (2021) https://doi.org/10.1038/s41558-021-01039-0 . Accessed 2022-09-22

Otto, A., Otto, F.E.L., Boucher, O., Church, J., Hegerl, G., Forster, P.M., Gillett, N.P., Gregory, J., Johnson, G.C., Knutti, R., Lewis, N., Lohmann, U., Marotzke, J., Myhre, G., Shindell, D., Stevens, B., Allen, M.R.: Energy budget constraints on climate response. Nature Geoscience **6**(6), 415–416 (2013) https://doi.org/10.1038/ngeo1836 . Accessed 2024-11-04

P. Ceppi, J.M.G.: A refined model for the earth's global energy balance. Nature Climate Dynamics **53**(7-8) (2019) https://doi.org/10.1007/s00382-019-04825-x . Accessed 2019-05-28

Proistosescu, C., Donohoe, A., Armour, K.C., Roe, G.H., Stuecker, M.F., Bitz, C.M.: Radiative Feedbacks From Stochastic Variability in Surface Temperature and Radiative Imbalance. Geophysical Research Letters **45**(10), 5082–5094 (2018) https://doi.org/10.1029/2018GL077678 . Accessed 2021-08-25

Proistosescu, C., Huybers, P.J.: Slow climate mode reconciles historical and model-based estimates of climate sensitivity. Science Advances **3**(7), 1602821 (2017) https://doi.org/10.1126/sciadv.1602821 . Accessed 2022-11-07

Rayner, N.A., Parker, D.E., Horton, E.B., Folland, C.K., Alexander, L.V., Rowell, D.P., Kent, E.C., Kaplan, A.: Global analyses of sea surface temperature, sea ice, and night marine air temperature since the late nineteenth century. JGR Atmospheres **108**(D14) (2003) https://doi.org/10.1029/2002JD002670 . Accessed 2003-07-17

Schmidt, G.A., Andrews, T., Bauer, S.E., Durack, P.J., Loeb, N.G., Ramaswamy, V., Arnold, N.P., Bosilovich, M.G., Cole, J., Horowitz, L.W., Johnson, G.C., Lyman, J.M., Medeiros, B., Michibata, T., Olonscheck, D., Paynter, D., Raghuraman, S.P., Schulz, M., Takasuka, D., Tallapragada, V., Taylor, P.C., Ziehn, T.: CERESMIP: a climate modeling protocol to investigate recent trends in the Earth's Energy Imbalance. Frontiers in Climate **5**, 1202161 (2023) https://doi.org/10.3389/fclim.2023.1202161 . Accessed 2024-11-04

Sherwood, S.C., Webb, M.J., Annan, J.D., Armour, K.C., Forster, P.M., Hargreaves, J.C., Hegerl, G., Klein, S.A., Marvel, K.D., Rohling, E.J., Watanabe, M., Andrews, T., Braconnot, P., Bretherton, C.S., Foster, G.L., Hausfather, Z., Heydt,

A.S., Knutti, R., Mauritsen, T., Norris, J.R., Proistosescu, C., Rugenstein, M., Schmidt, G.A., Tokarska, K.B., Zelinka, M.D.: An Assessment of Earth's Climate Sensitivity Using Multiple Lines of Evidence. Reviews of Geophysics **58**(4) (2020) https://doi.org/10.1029/2019RG000678 . Accessed 2021-08-28

Webb, M.J., Andrews, T., Bodas-Salcedo, A., Bony, S., Bretherton, C.S., Chadwick, R., Chepfer, H., Douville, H., Good, P., Kay, J.E., Klein, S.A., Marchand, R., Medeiros, B., Siebesma, A.P., Skinner, C.B., Stevens, B., Tselioudis, G., Tsushima, Y., Watanabe, M.: The Cloud Feedback Model Intercomparison Project (CFMIP) contribution to CMIP6. Geoscientific Model Development **10**(1), 359–384 (2017) https://doi.org/10.5194/gmd-10-359-2017 . Accessed 2024-04-05

Zhou, C., Zelinka, M.D., Klein, S.A.: Impact of decadal cloud variations on the Earth's energy budget. Nature Geoscience **9**(12), 871–874 (2016) https://doi.org/10.1038/ngeo2828 . Accessed 2021-10-25

Zhou, C., Zelinka, M.D., Klein, S.A.: Analyzing the dependence of global cloud feedback on the spatial pattern of sea surface temperature change with a green's function approach. Journal of Advances in Modeling Earth Systems **9**(5), 2174–2189 (2017) https://doi.org/10.1002/2017MS001096 . Accessed 2021-08-25

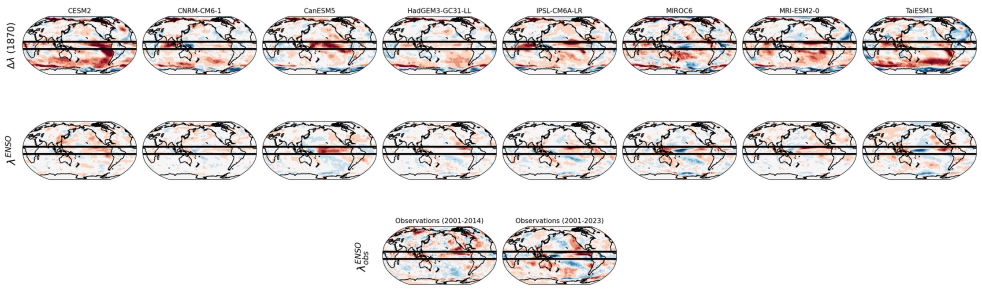

Fig. 1 Depiction of the bounding box (global 10N to 10S) used to calculate the correlation between pattern effect and ENSO feedback spatial patterns in Table S1.

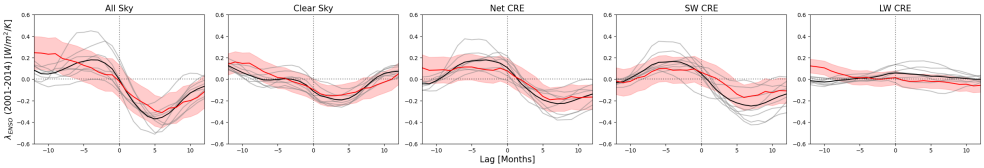

Fig. 2 Comparison between modeled ENSO feedbacks (grey), the model ensemble average (black) and observed ENSO feedbacks (red), with the red shaded area representing the 95-percentile confidence interval for observations. Positive lags indicate nino3.4 leads.

Model	r Model λ_{ENSO} and $\Delta\lambda$	r $\lambda_{ENSO,Obs2014}$ and $\Delta\lambda$	r $\lambda_{ENSO,Obs2023}$ and $\Delta\lambda$
CESM2	0.52	0.51	0.64
CNRM-CM6-1	0.59	0.8	0.83
CanESM5	0.57	0.63	0.62
HadGEM3-GC31-LL	0.4	0.5	0.55
IPSL-CM6A-LR	0.71	0.7	0.75
MIROC6	0.44	0.48	0.59
MRI-ESM2-0	0.57	0.55	0.64
TaiESM1	0.54	0.52	0.62

Table 1 Table depicting the correlation within a global 10N-10S bounding between modeled pattern effect ($\Delta\lambda$) and (column 2) modeled ENSO feedback, (column 3) observed ENSO feedback (2001-2014), and (column 4) observed ENSO feedback (2001-2023).

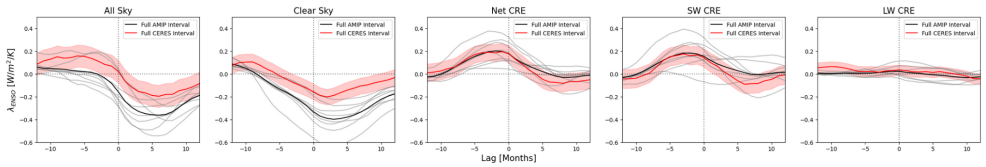

Fig. 3 Comparison between the full AMIP-interval ENSO feedbacks for each CMIP model (grey), the model ensemble average (black) and full CERES-interval ENSO feedbacks (red), with the red shaded area representing the 95-percentile confidence interval for observations. Positive lags indicate nino3.4 leads.